Bayesian sea ice detection with the Advanced Scatterometer

Maria Belmonte Rivas, Jeroen Verspeek, Anton Verhoef, Ad Stoffelen

Abstract— **This paper details the construction of a Bayesian sea ice detection algorithm for the C-band Advanced Scatterometer ASCAT on board MetOp based on probabilistic distances to ocean wind and sea ice Geophysical Model Functions (GMFs). The performance of the algorithm is validated against coincident active and passive microwave sea ice extents on a global scale across the seasons. The comparison between the ASCAT, QuikSCAT and AMSR-E records during 2008 is satisfactory during the winter seasons, but reveals systematic biases between active and passive microwave methods during the summer months. These differences arise from their different sensitivities to mixed sea ice and open water conditions, scatterometers being more inclusive regarding the detection of lower concentration and summer ice. The sea ice normalized backscatter observed at C-band shows some loss of contrast between thin and thick ice types relative to the Ku-band QuikSCAT, but offers a better sensitivity to prominent surface features, such as fragmentation and rafting of marginal sea ice.**

Index Terms— **Sea ice, Bayes procedures, microwave scatterometry, microwave radiometry, radar scattering.**

I. INTRODUCTION

THE polar regions remain a central focus of many climate change studies in recent years, both because of the large amount of changes observed by satellite sensors [1, 2] and because of the expectations of amplified weather and climate signals due to feedback effects [3, 4]. These studies underscore the importance of an accurate sea ice description in the assessment of the impact that sea ice variability can pose on local and remote climates around the world [5]. The accurate and dependable discrimination between open ocean and sea ice areas also constitutes an operational demand for a suite of satellite based retrievals of ocean properties, including surface winds [6], sea surface temperatures [7], ocean color [8] and sea surface heights [9]. Although the acquisition of daily Arctic and Antarctic sea ice extents has been historically mediated by satellite microwave radiometers [10], novel scatterometer methods have emerged that prove as robust [11, 12, 21, 22]. The utility of satellite active microwave sensors to map sea ice extents and thickness, which continue to be objects of interest [13], has been demonstrated with the development of

a Bayesian sea ice detection algorithm for QuikSCAT [12, 25] that is capable of revealing seasonal extent errors of up to 20% in passive microwave records, mainly caused by undetected low concentration and soaked sea ice conditions [14, 15]. Using the same Bayesian methodology, this work investigates the sea ice mapping capabilities of the Advanced Scatterometer (ASCAT) on board MetOp, and assesses the possibility of a continuous scatterometer sea ice record after the operational termination of the QuikSCAT sensor in November 2009.

Section II details the construction and underlying principles of the Bayesian sea ice detection algorithm for the ASCAT scatterometer on MetOp. In Section III, we examine the location of the resulting sea ice edge against sea ice extents measured by QuikSCAT and sea ice concentrations derived from the standard AMSR-E (Advanced Microwave Scanning Radiometer) Enhanced NASA Team (NT2) algorithm during 2008. Section IV summarizes our results and concludes with notes on future work.

II. ALGORITHM DESCRIPTION

Scatterometers are active microwave sensors designed for the global determination of ocean surface wind vectors. The C-band Advanced Scatterometer ASCAT on board MetOp [16] flies on a sun-synchronous orbit at 830 km altitude with ascending node at 9.30PM and a 29-day repeat cycle. It radiates microwave pulses at a frequency of 5.3 GHz and employs a total of six fan-beam antennas (three on each side) oriented at 45°, 90° and 135° relative to the satellite track for the reception of vertically polarized returns from a variety of incidence angles (Fig.1). The antenna beam footprints cover a total swath of 2 x 550 km across-track divided into 25 km grid nodes (50 km nominal resolution) each collecting one triplet of average backscatter measurements $\{\sigma^0_{FORE}, \sigma^0_{AFT}, \sigma^0_{MID}\}$ per satellite pass. The observation geometry is a function of across-track node position (or WVC number, Wind Vector Cell) with surface incidence angles ranging from 25° to 53° for the MID beam and 34° to 64° for the AFT and FORE antennas. The multi-look nature of these observations is essential to the retrieval of the wind vector signature (wind speed and direction) over the ocean surface. The Bayesian discrimination algorithm relies on prior knowledge about the expected (i.e. average) location and dispersion of the sea ice and open water backscatter populations in the ASCAT measurement space. This prior knowledge is conveyed by empirical Geophysical Model Functions (GMFs) for ocean wind and sea ice backscatter at C-band.
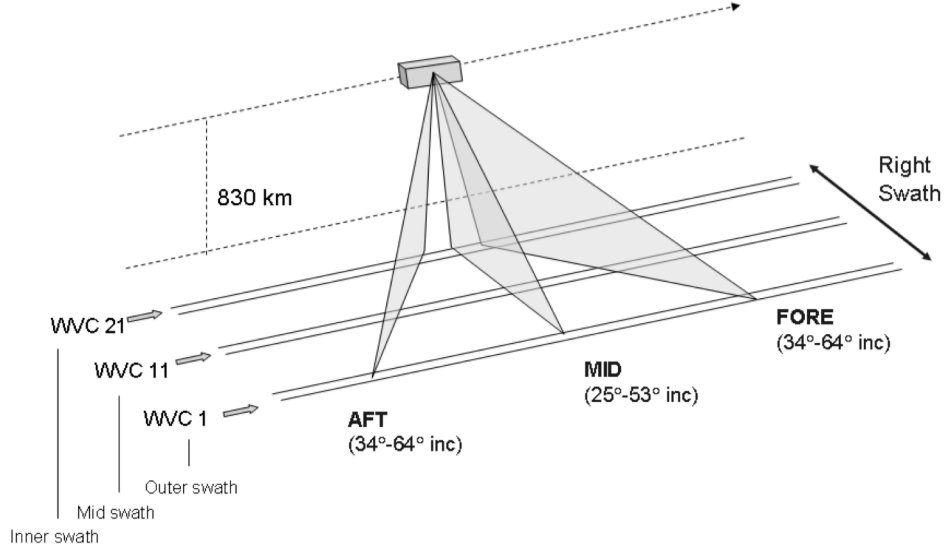
Fig. 1. ASCAT observation geometry. The right and left swaths (left not shown) are gridded into resolution nodes (Wind Vector Cells, WVCs) collecting one triplet of averaged σ^0_{FORE}, σ^0_{AFT}, σ^0_{MID} backscatter measurements per node. The incidence angle at the surface depends on the node position, ranging from 25° to 53° for the MID antenna and from 34° to 64° for the AFT and FORE antennas.

The ocean wind GMF for vertical polarization, denoted CMOD5 [17], is an empirical relation derived on the basis of measurements from the European Remote Sensing Satellite ERS2 scatterometer and first-guess winds from the European Centre for Medium-Range Weather Forecasts (ECMWF). The CMOD5 GMF has been tested extensively on ASCAT data with operational wind products as final result, and proposed as a means towards ASCAT calibration [26]. Shown in Fig. 2, the ocean wind backscatter conforms to a two-dimensional cone-shaped manifold in the three-dimensional space of ASCAT $\{\sigma^0_{FORE}, \sigma^0_{AFT}, \sigma^0_{MID}\}$ measurements. Its precise formulation changes with observation geometry (across-track location WVC) and features wind speed v and direction ϕ as independent variables:

$$\sigma^0_{wind} = CMOD5(v, \phi, WVC) \tag{1}$$

The empirical GMF for sea ice σ^0_{ice} has been drawn from the observed distribution of sea ice backscatter during the wintertime. We use wintertime data because it is representative of 100% sea ice concentration and leads to more compact model fits. The underlying assumption is that the wintertime sea ice model remains valid all year round, while summer departures from the wintertime model are to be attributed to mixed surface conditions, which include lower concentration and melting sea ice. The sea ice backscatter GMF is azimuth (and nearly WVC) invariant, featuring sea ice normalized backscatter or "proxy ice age" as independent variable, and conforming to a one-dimensional straight line in the three-dimensional

ASCAT dB-space, also plotted in Fig. 2. The sea ice and ocean wind GMFs shown in Fig. 2 encapsulate our statistical knowledge about the expected distributions of sea ice and ocean wind backscatter populations all year round in both northern and southern hemispheres – i.e. they don't change with time or geographical location.
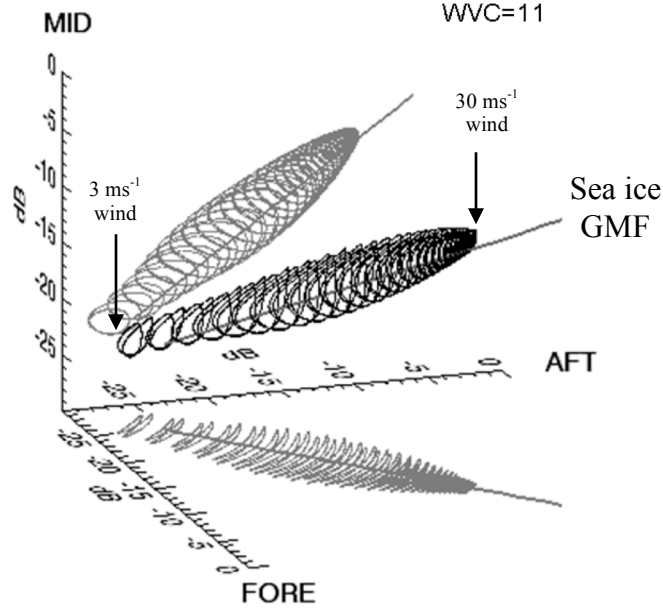

Fig. 2. Geophysical Model Functions (GMFs) for ocean wind and sea ice backscatter at C-band V-pol in the three-dimensional space of ASCAT measurements for a mid-swath WVC. The ocean wind GMF is a tube-shaped manifold depicted here as a function of wind speed (3-30 ms^{-1} in steps of 1 ms^{-1}) and direction. The sea ice GMF is a straight line with azimuthal (AFT/FORE) symmetry, depicted as a function of sea ice normalized backscatter.

The sea ice GMF at C-band can be approximately expressed in parametric form as:

$$\sigma_{ice}^0 \Rightarrow \begin{cases} \sigma_{ice,FORE}^0 = \sigma_{ice,AFT}^0 \\ \sigma_{ice,MID}^0 = 0.7 + 0.925 \cdot \sigma_{ice,FORE}^0 \end{cases} \qquad (2)$$

The first relation in (2) expresses the fact that, unlike ocean wind backscatter, sea ice backscatter shows no directional preference in azimuth (σ_{FORE}^0 and σ_{AFT}^0 illuminate the surface at identical incidence angles but 90° apart in azimuth) [23]. The second relation, which gives the slope of the iceline in the ASCAT dB-space, relates backscatter at two nearby incidence angles (σ_{FORE}^0 and σ_{MID}^0 illuminate the surface with ~10° separation in incidence angle) and implies that the derivative of backscatter with incidence angle (which is proportional to $\sigma_{FORE}^0 - \sigma_{MID}^0$) increases linearly (becomes less negative) with sea ice backscatter, reflecting the fact that smoother new ice surfaces show steeper backscatter derivatives than older and more lambertian sea ice types, as illustrated in Fig.3. The discrimination between sea ice and open water is based on the separability of their respective backscatter signatures, but the relative location of the ocean wind and sea ice

backscatter GMFs in the ASCAT measurement space is a function of across-track position, as the location

of the wind cone shifts with the observation geometry from inner to outer WVCs.
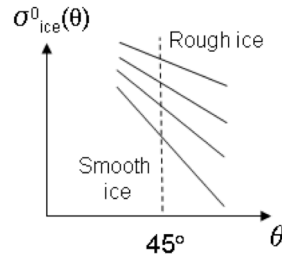
Fig. 3. Physical interpretation of the sea ice GMF slope (for wintertime 100% concentration sea ice, marginal sea ice excluded):
The derivative of backscatter with respect to incidence angle becomes more positive for older and brighter sea ice types.
This interpretation holds for incidence angles between 25 and 64 degrees. See Fig.15 in [24]

Figure 4 shows the relative locations of the average ocean wind and sea ice backscatter populations as a

function of WVC number, along with a cloud of actual sea ice backscatter points illustrating the dispersion

of measurements about the sea ice model. Shown are the 2D projections onto "side view" (sigma0_fore =

sigma0_aft) and "top view" (sigma0_mid = 0) planes defined in the 3D space of ASCAT measurements

(see Figure 2).
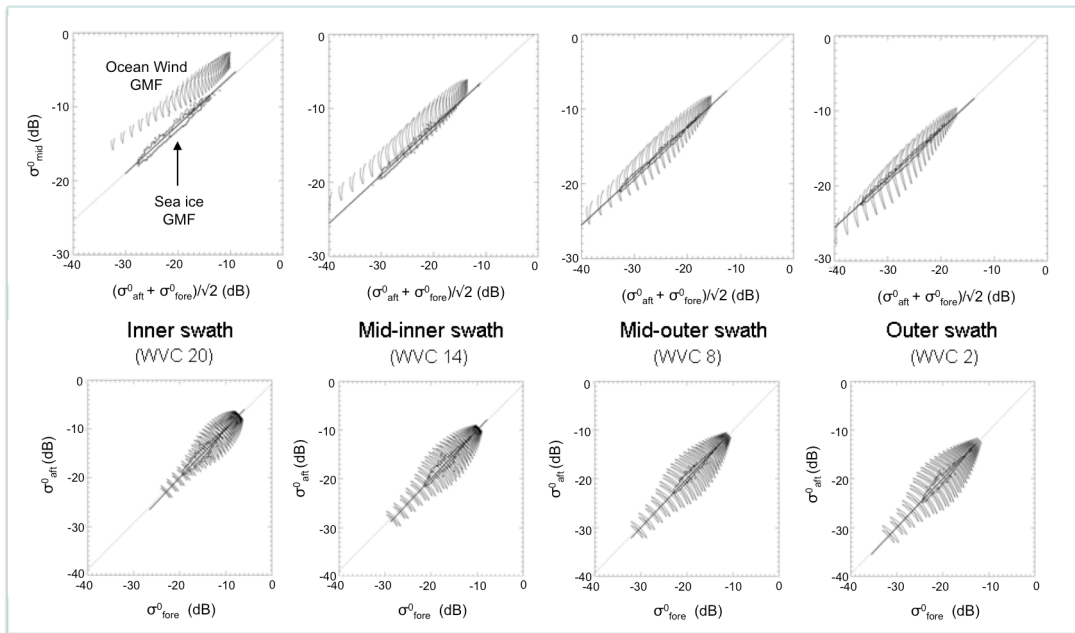
Fig. 4. Geophysical Model Functions (GMFs) for ocean wind and sea ice backscatter at C-band in the three-dimensional space of ASCAT
measurements as a function of across-track position (WVC number). The GMFs are projected onto the $\sigma^0_{FORE} = \sigma^0_{AFT}$ plane (side view, TOP
row) and the $\sigma^0_{MID} = 0$ plane (top view, BOTTOM row) for inner, mid-inner, mid-outer and outer swath WVCs.

The sea ice GMF lies under the ocean wind GMF over the inner swath cells, implying that open ocean

returns feature steeper backscatter derivatives than sea ice returns at small incidence angles. Physically,

large differences in backscatter slope and azimuthal response ensure the good separability of sea ice and open water cells over the ASCAT inner swath. Over the outer swath, the sea ice GMF lies inside the wind cone, indicating that backscatter slopes become more similar at large incidence angles, but the azimuthal modulation of ocean returns is also amplified, suggesting that the separability of sea ice and open water relies more heavily on their different azimuthal responses at large incidence angles. Observe that class discrimination is compromised in cases for which the ocean wind and sea ice GMFs intersect one another, as occurs over the ASCAT mid-inner swath cells. In these cases, sea ice returns happens to bear a signature identical to that of an along-track ocean wind, and the discrimination between sea ice and open water left to be solved by contextual information, like historic priors from previous satellite passes or Numerical Weather Prediction (NWP) model constraints. The Bayesian posterior sea ice probability is formulated as:

$$p(ice \mid \sigma^0) = \frac{p(\sigma^0 \mid ice)p_0(ice)}{p(\sigma^0 \mid ice)p_0(ice) + p(\sigma^0 \mid wind)p_0(wind)} \tag{3}$$

In terms of historic prior information $p_0(ice)$ and $p_0(wind)$ (to be defined later in this section), and the conditional probability distributions of minimum squared distances $p(\sigma^0|wind)$ and $p(\sigma^0|ice)$ to sea ice and ocean wind model functions, defined as:

$$p(\sigma^0 \mid ice) = p(MLE_{ice})$$

$$p(\sigma^0 \mid wind) = p(MLE_{wind}) \tag{4}$$

To calculate the Bayesian sea ice and ocean wind conditional probability functions in Eq. (4), we define the expected dispersion of data about the respective class GMFs using a normalized measure of distance, denoted minimum square distance (or MLE, from Maximum Likelihood Estimator) and expressed as:

$$MLE_{wind} = \min\left\{ \sum_{i=1,\ldots,N} (\sigma_i^0 - \sigma_{wind,i}^0)^2 / \mathrm{var}[\sigma_{wind,i}^0] \right\} \tag{5}$$

$$MLE_{ice} = \min\left\{ \sum_{i=1,\ldots,N} (\sigma_i^0 - \sigma_{ice,i}^0)^2 / \mathrm{var}[\sigma_{ice,i}^0] \right\} \tag{6}$$

where i is an index to the components of the backscatter vector and N its dimension (N = 3 for ASCAT). The distance minimization, also known as GMF fitting procedure, is performed across the two-dimensional space of model wind speed and directions in Eq.(5), and across the one-dimensional space of model sea ice normalized backscatter or "proxy ice age" in Eq.(6). The normalizing factors $\mathrm{var}[\sigma^0_{class,i}]$ ensure that the variance of backscatter components σ^0_i about the corresponding model function, σ^0_{wind} or σ^0_{ice}, is unity. The variance of measurements about the ocean wind GMF is a well known parameter and is expressed as the

sum of instrumental K_p and geophysical MLE_{geo} random Gaussian components as:

$$\text{var}[\sigma^0_{wind}] = MLE_{geo}(K_p \sigma^0_{wind})^2 \tag{7}$$

The term K_p noise refers to instrumental (radiometric + fading) noise, with a best case value of 4% at high winds (50 km resolution). The geophysical MLE_{geo} noise is a lumped concept that accounts for perturbations in ocean wind backscatter that cannot be attributed to instrumental noise, such as wind variability, atmospheric instability or undetected rain [18] with a best case value of 4% at high winds. The variance of sea ice backscatter about the sea ice GMF is also commensurate with instrumental noise, but features a seasonally varying component that depends on the presence of mixed sea ice and open water conditions (i.e pixels that share both volumetric sea ice and surface ocean backscatter signatures) in a resolution cell, and is expressed as:

$$\text{var}[\sigma^0_{ice}] = C_{mix}(K_p \sigma^0_{ice})^2 \tag{8}$$

The tolerance parameter C_{mix}, which deals with excursions away from the sea ice model than cannot be attributed to instrumental noise, will be tuned empirically against independent data in the next section. Assuming random Gaussian perturbations in the backscatter components measured by ASCAT, one may write the Bayesian conditional probability functions for ocean wind and sea ice backscatter observations, $p(MLE_{wind})$ and $p(MLE_{ice})$, as chi-square functions with $Q = N - 2$ and $Q = N - 1$ degrees of freedom, where Q is the number of linear constraints imposed by the distance minimization procedure:

$$p(MLE_{wind}) = \chi^2_{Q=1}(MLE_{wind}) = \frac{\exp(-MLE_{wind}/2)}{\sqrt{2\pi MLE_{wind}}} \tag{9}$$

$$p(MLE_{ice}) = \chi^2_{Q=2}(MLE_{ice}) = \frac{1}{2}\exp(-MLE_{ice}/2) \tag{10}$$
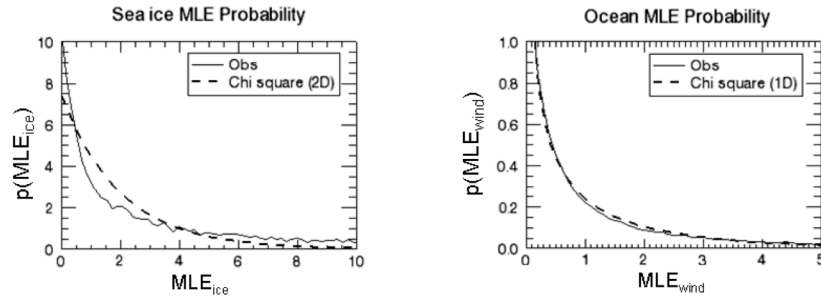
Fig. 5. Observed (continuous) and modeled (dashed) MLE distributions to sea ice (LEFT) and ocean wind (RIGHT) model functions. For reference, the instrumental noise standard deviation used to generate these figures is $K_p \sim 4\%$ (or about 0.15 dB) and the sea ice tolerance factor Cmix ~ 3.

The actual and expected distributions of minimum squared distances MLE to the 2D ocean wind and 1D

sea ice GMFs are shown in Figure 5. The observed MLE distributions follow the expected chi-square functions closely, justifying our starting assumptions.

The classification deficiencies associated with the fact that class GMFs are bound to intersect over the swath (i.e. for mid-inner swath WVCs) are to be overcome using a combination of prior probability updates from previous satellite passes, and constraints based on Numerical Weather Prediction (NWP) forecasts of the surface wind v_{NWP}. The prior sea ice and ocean wind probabilities in Eq.(3) are set initially to $p_0(ice) = 0.35 = 1 - p_0(wind)$ and updated every orbit using the posteriors from the previous pass:

$$p_0(ice) = p(ice \,|\, \sigma^0) = 1 - p_0(wind) \tag{11}$$

This initial prior setting is rather inconsequential, as neither results nor algorithm convergence (~5 days) are sensitive to it. Once a day, the posterior $p(ice|\sigma^0)$ is smoothed spatially with a Gaussian filter (17 km width) and the resulting prior relaxed towards uncertainty to prevent the Bayesian filter from saturation:

$$p_0(ice) = \begin{cases} 0.50 & if \ p(ice \,|\, \sigma^0) > 0.70 \\ 0.15 & if \ p(ice \,|\, \sigma^0) < 0.70 \end{cases} \tag{12}$$

The conditional ocean wind probabilities in Eq.(9) are constrained by ECMWF short-range wind forecasts v_{NWP} to prevent sea ice points lying close to the ocean GMF from being classified as open water when the apparent surface wind deviates largely from the NWP forecast:

$$p(\sigma^0 \,|\, wind) = p(MLE_{wind}) \cdot \exp\left[-(\vec{v} - \vec{v}_{NWP})^2 / (2 \cdot \Delta v_{NWP}^2)\right] \tag{13}$$

where $\Delta v_{NWP} = 2 \ ms^{-1}$. These settings are found to optimize the amount of prior and actual information fed into the algorithm, and efficient at inhibiting misclassification noise and filter saturation errors. The Bayesian algorithm implemented at the Royal Netherlands Meteorological Institute (KNMI) updates the ASCAT ice masks on a per pass basis for wind screening purposes, and produces a sea ice coverage map once a day on a 12.5 km polar stereographic grid using a 55% threshold to posterior sea ice probabilities in Eq.(3). The probability threshold was set slightly larger than the relaxed a priori sea ice probability at 50%: mark, however, that the sea ice maps are only marginally sensitive to this parameter, being mainly responsive to changes in the tolerance parameter C_{mix}. The sea ice maps are filled with normalized backscatter values, which are a qualitative proxy for sea ice age/thickness [23, 24] (see Figure 10) and finally archived.

III. ALGORITHM TUNING AND VALIDATION

As validation datasets, we use the continuous series of daily sea ice extents recorded by QuikSCAT and the passive microwave AMSR-E sensor in the period spanning from January through December 2008. The QuikSCAT sea ice extents have been derived from the KNMI Bayesian sea ice detection algorithm [12]. The passive microwave sea ice extents are defined by the 15% threshold on sea ice concentrations generated by the Enhanced NASA Team NT2 algorithm (AE SI12 Version 1) [19].

As a preliminary step, the ASCAT sea ice classifier is adjusted to a suitable reference using the tolerance factor C_{mix} as tuning parameter. Recall that the tolerance factor provides a margin for the expected (thus acceptable) geophysical departures of sea ice backscatter from the wintertime sea ice model, which may be legitimately caused by mixed sea ice and open water conditions in a resolution cell, or else attributed to rain contamination. The ASCAT sea ice detection algorithm has been run using a discrete range of tolerance factor values (C_{mix} = 1, 2, 3) and the results are shown in Fig. 6 for the Northern and Southern Hemispheres. The total extent of sea ice detected by ASCAT naturally increases with the tolerance factor, but this sensitivity is geographically confined to areas with frequent mixed sea ice and open water conditions, such as the Arctic ice edge in the summer, and the Antarctic ice margin all year round.
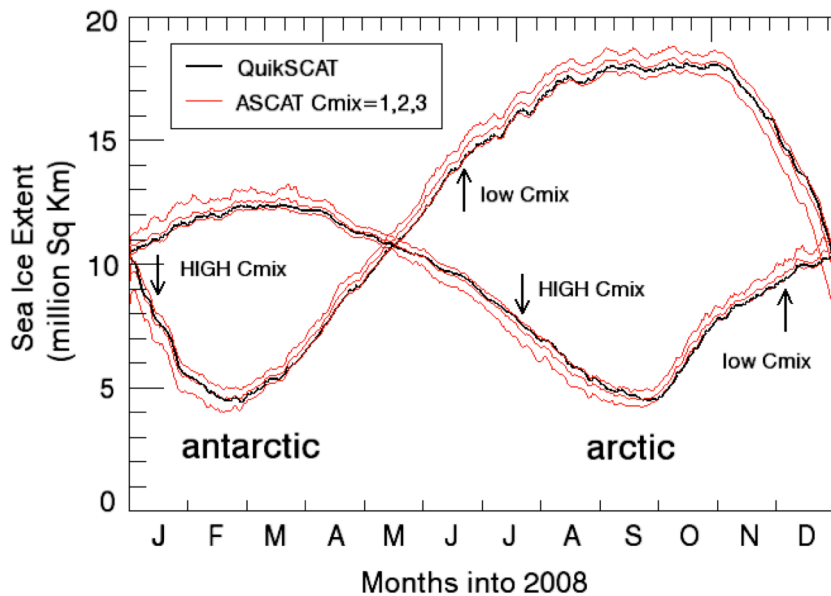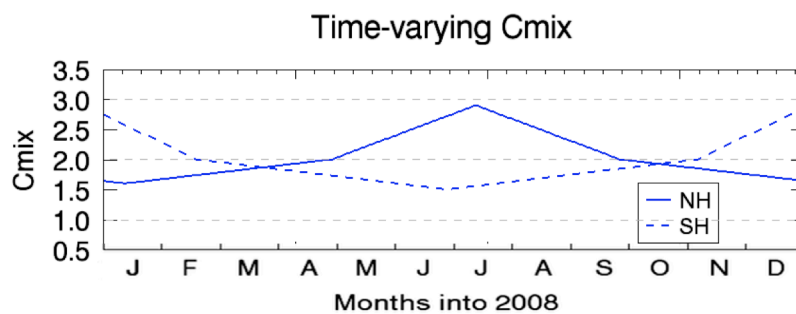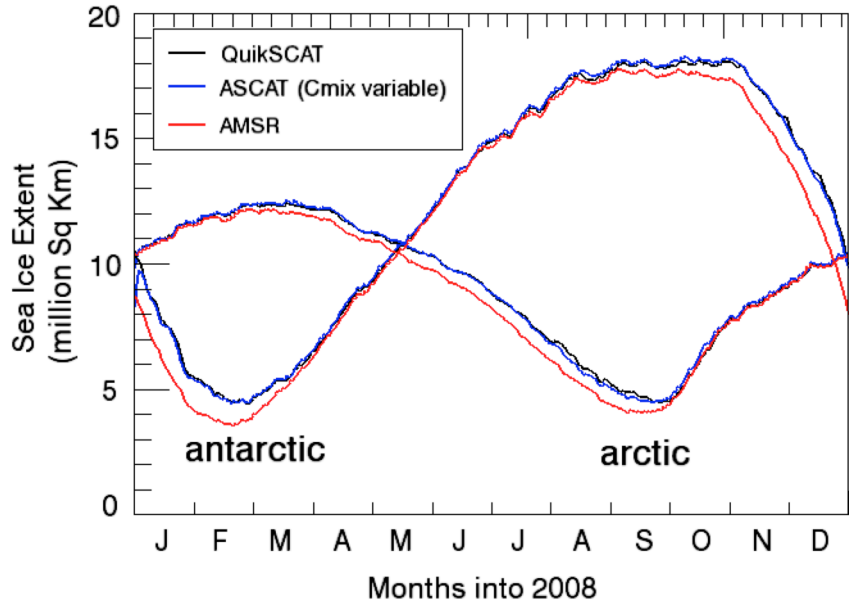

Fig. 6 Daily Arctic and Antarctic sea ice extents from Jan'08 through Dec'08
from QuikSCAT (black line) and ASCAT (red lines) for Cmix = 1, 2 and 3.

The algorithm sensitivity during the winter months is aggravated by a dramatic response to rain contamination over open water areas, manifested as false sea ice positives. The volume scattering signature attributed to rain at C-band, although not as strong as at Ku-band, masks the directional response driven by the spectrum of surface waves and brings backscatter closer to the azimuthally flat signature that is characteristic of sea ice backscatter. Rain contamination is particularly present over open water areas subject to frequent and intense storminess like the Arctic latitudes in winter [20].

In general, we observe that low C_{mix} values give better agreement with QuikSCAT sea ice extents during the growth seasons, but prove deficient during the melt season. On the contrary, high C_{mix} values give better agreement during the melt season, but prove extremely noisy during the growth season. That is, the observed departures of sea ice backscatter from the wintertime sea ice model should remain small during the winter months, so that an increase in the tolerance parameter would only bring enhanced levels of misclassification noise (mostly from rain contamination associated with high latitude storms). During the summer months, the mixed sea ice conditions that predominate along the edge (low concentration and melting sea ice) push the signature of sea ice backscatter away from the wintertime sea ice model towards the ocean model, producing larger departures that need to be specially handled. A good compromise can be reached by using a time varying C_{mix} parameter that features low values in the winter (to suppress rain contamination in the absence of mixed sea ice and open water conditions) and high values in the summer (to favor the capture of low concentration and flooded sea ice).

Fig. 7 Time varying scheme for the ASCAT tolerance parameter C_{mix} featuring high values in the summer and low values in winter.
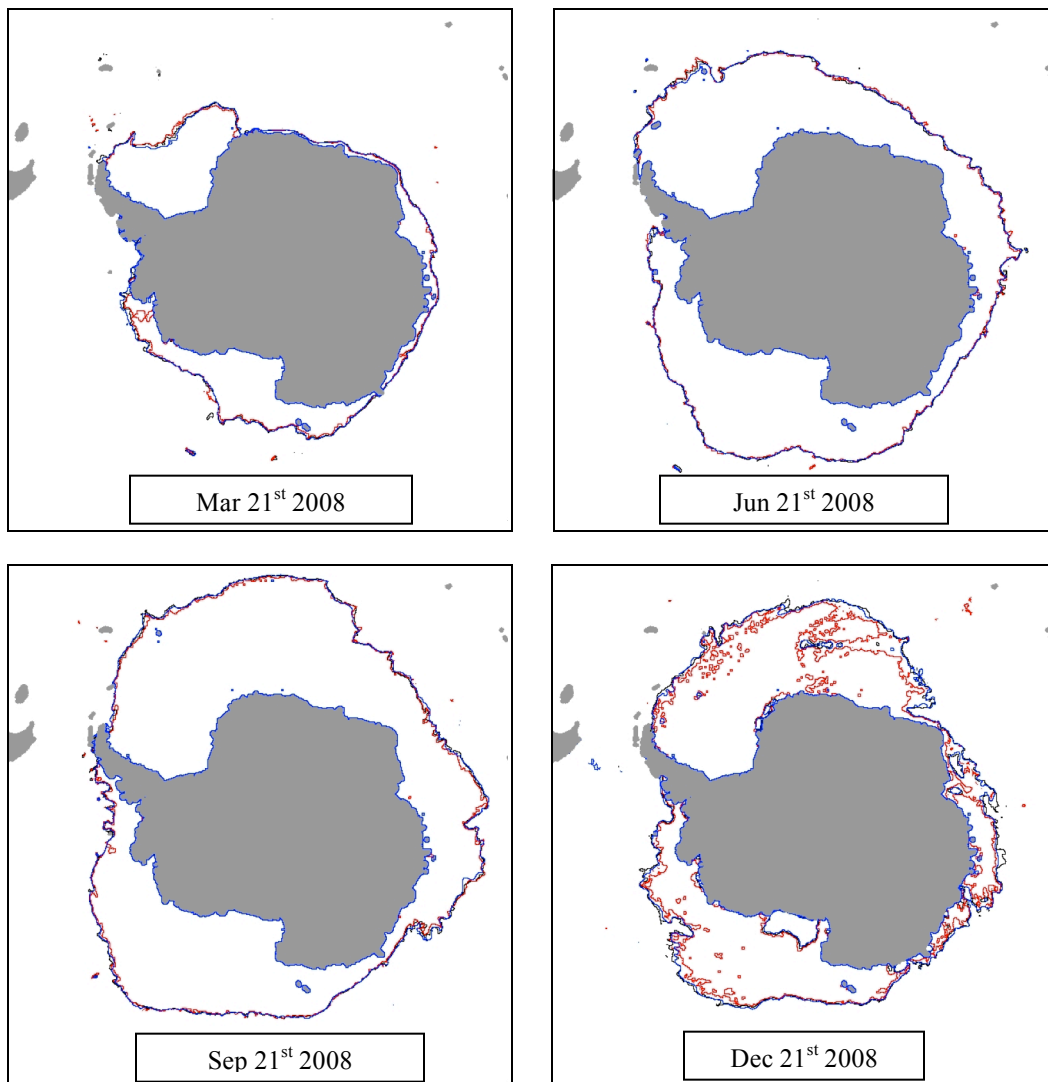
Fig. 8 Daily Arctic and Antarctic sea ice extents from Jan'08 through Dec'08
from QuikSCAT (black line), ASCAT (blue lines) and AMSR-R (red lines).
The ASCAT algorithm uses the time-varying C_{mix} scheme introduced in the text.

The time-varying C_{mix} scheme proposed is shown in Figure 7. The ASCAT sea ice extents that result from this configuration are compared against QuikSCAT and AMSR-E observations in Figure 8. We observe an excellent agreement among all three algorithms during the ice growth seasons (ascending branches in Fig.8), but notice remarkable discrepancies between active and passive microwave extents during the melt months (descending branches in Fig.8). The internal agreement between ASCAT and QuikSCAT sea ice extents remains very good all year round, supporting the ability of ASCAT to provide a smooth continuation to the existing long-term scatterometer sea ice record established by QuikSCAT. The discrepancies between the active and passive microwave methods are indicative of their differing ability to detect mixed sea ice and open water conditions [12], and confirm the proficient capabilities of scatterometers to monitor spring and summer sea ice.

Figures 9a and 9b illustrate the seasonal and geographical behavior of the ASCAT, QuikSCAT and AMSR-E (15% concentration threshold) sea ice masks for a limited subset of days. Within the limits imposed by misclassification noise and temporal sea ice variability, all three algorithms are found to show best agreement during the winter seasons (i.e. December in the Northern Hemisphere, June and September in

the Southern Hemisphere), with discrepancies between active and passive techniques becoming more pronounced during the summer months (December in the Southern Hemisphere, June and September in the Northern Hemisphere). The agreement between the sea ice edges derived from QuikSCAT and ASCAT is very good all year round, although we notice that summer sea ice detection with ASCAT is slightly inferior to QuikSCAT's, which we take to be the best summer reference after extensive validation against high resolution radar and visible maps [12]. The differences in summer sea ice detection between ASCAT and QuikSCAT may be attributed to the relative locations of the sea ice and ocean wind GMFs in their respective measurement spaces, along with different observations densities over a day – giving advantage to QuikSCAT's larger swath width.

Fig. 9b Daily Antarctic sea ice extents from QuikSCAT (black line), ASCAT (blue lines) and AMSR-R (15% concentration, red lines).
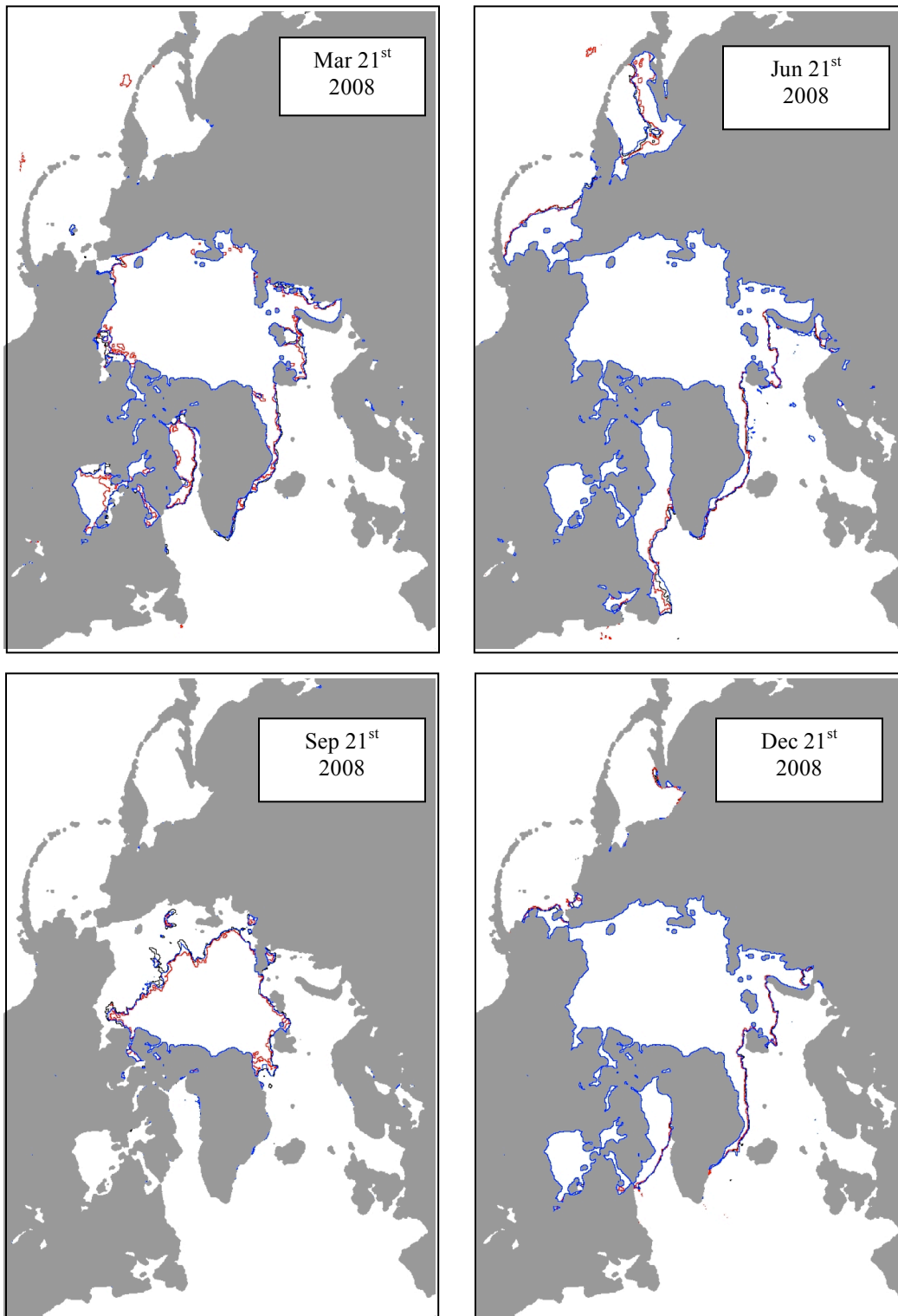
Fig. 9a Daily Arctic sea ice extents from QuikSCAT (black line), ASCAT (blue lines) and AMSR-R (15% concentration, red lines).

Figures 10 and 11 show the final ASCAT sea ice products, daily sea ice masks filled with sea ice normalized backscatter values (as qualitative proxies for "ice age/thickness") calculated after mapping the observed ASCAT backscatter to a mid-swath reference node for March 21st (Northern Hemisphere) and September 21st 2008 (Southern Hemisphere). The normalization of ASCAT backscatter to the reference mid-swath node (WVC = 11, or about 41° incidence for the mid beam) is effected by scaling the projection of the observed backscatter vector onto the sea ice model unit vector as:

$$a = [\sigma^0_{fore}, \sigma^0_{aft}, \sigma^0_{mid}] \cdot \vec{u}_{ice} \tag{14}$$

$$a_{normalized} = (a - <a_{WVC}>) \cdot STD_a(WVC = 11) / STD_a$$

where $\mathbf{u}_{ice}$ = [0.594, 0.594, 0.542] is the sea ice model unit vector and Table 1 details the normalization coefficients $<a_{WVC}>$ and STD_a, representing the centroid and standard deviation of the sea ice backscatter projections along the sea ice line as a function of WVC. This procedure effectively eliminates the dependence of ASCAT normalized backscatter on incidence angle (i.e. cross-track location).

Table 1 – Coefficients for the normalization of ASCAT backscatter

WVC	Incidence (mid/fore)	$<a_{WVC}>$ (dB)	$STD_a(WVC)$ (dB)
1	51.8° / 63.0°	-32.00	4.17
2	50.8° / 62.1°	-31.83	4.17
3	49.8° / 61.1°	-31.64	4.17
4	48.8° / 60.1°	-31.43	4.16
5	47.8° / 59.1°	-31.22	4.15
6	46.7° / 58.0°	-30.97	4.14
7	45.6° / 56.9°	-30.70	4.12
8	44.5° / 55.7°	-30.40	4.10
9	43.3° / 54.5°	-30.09	4.07
10	42.1° / 53.2°	-29.74	4.04
11	40.9° / 51.9°	-29.37	4.01
12	39.6° / 50.6°	-29.00	3.98
13	38.3° / 49.2°	-28.57	3.94
14	36.9° / 47.7°	-28.11	3.90
15	35.6° / 46.1°	-27.63	3.86
16	34.1° / 44.6°	-27.14	3.83
17	32.7° / 42.9°	-26.62	3.79
18	31.2° / 41.2°	-26.08	3.76
19	29.7° / 39.4°	-25.52	3.73
20	28.1° / 37.5°	-24.93	3.71
21	26.5° / 35.6°	-24.35	3.69
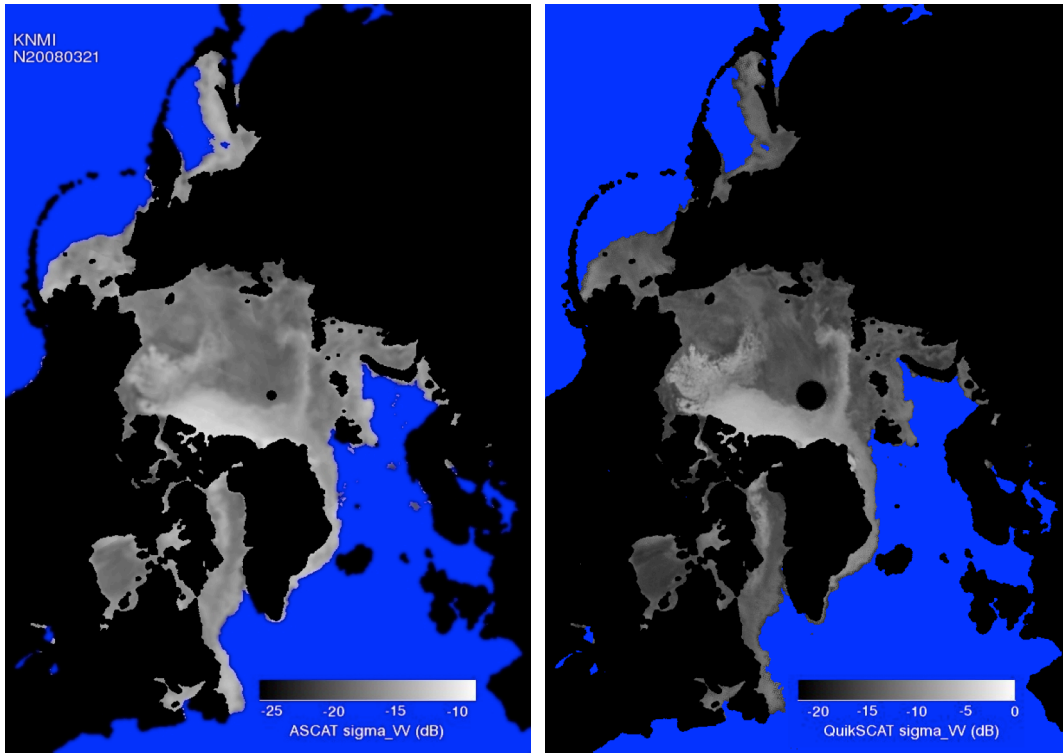
ASCAT **QuikSCAT**

Fig. 10 Arctic sea ice extents from C-band ASCAT (left) and Ku-band QuikSCAT (right) on March 21st 2008
Background grey scale represents sea ice normalized VV backscatter (ASCAT mapped to WVC=11 or about 41° incidence).
ASCAT and QuikSCAT data resolution is 50 km. The map gridding is 12.5 km.
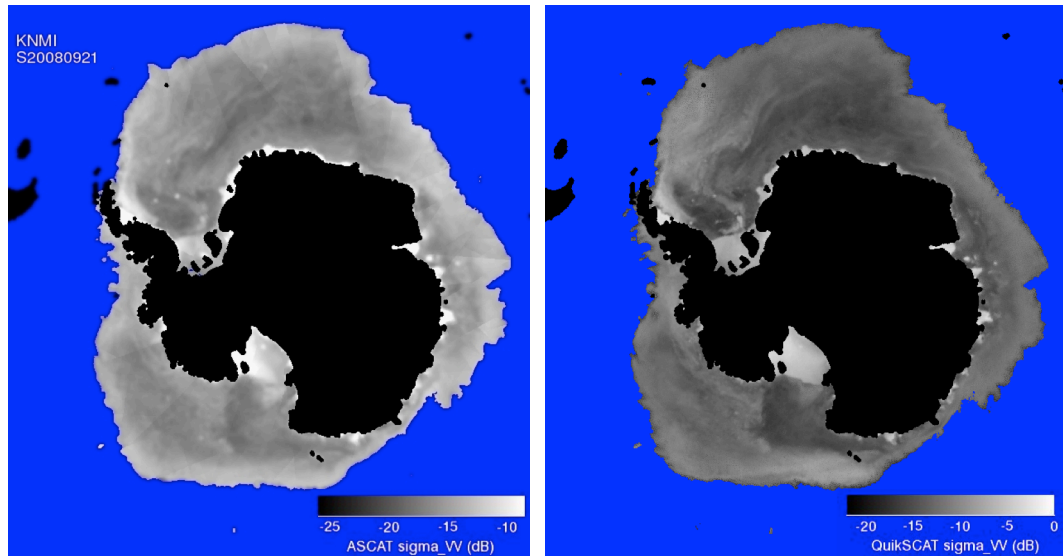
ASCAT **QuikSCAT**

Fig. 11 Antarctic sea ice extents from C-band ASCAT (left) and Ku-band QuikSCAT (right) on September 21st 2008
Background grey scale represents sea ice normalized VV backscatter strength (ASCAT mapped to WVC=11 or about 41° incidence).
ASCAT and QuikSCAT data resolution is 50 km. The map gridding is 12.5 km.

The comparison against the Ku-band sea ice backscatter from QuikSCAT shown in Fig.10 indicates that the contrast between bright multiyear and dimmer first year ice (thus their separability) appears to be stronger in the QuikSCAT case, whereas ASCAT appears to collect a larger response from the marginal ice zones. Not surprisingly, the longer illumination wavelength at C-band (~ 5 cm) is expected to be more responsive to surface features, such as rafted/fragmented sea ice along the margins, and less responsive to volume scattering features, such as air and brine pockets in multiyear ice, than illumination at Ku-band (~ 2 cm).

IV. SUMMARY AND CONCLUSIONS

This paper details the construction of a Bayesian sea ice detection algorithm for the C-band Advanced Scatterometer ASCAT on board MetOp. The algorithm relies on the statistical characterization of the backscatter from sea ice and wind roughened ocean surfaces articulated via Geophysical Model Functions. The performance of the new algorithm is validated against coincident active and passive microwave sea ice extents on a global scale and across the seasons. The agreement between the ASCAT, QuikSCAT and AMSR-E records during 2008 is satisfactory during the winter season, although the comparison reveals systematic biases between active and passive microwave methods during the summer months. These differences seem to arise from different sensitivities to mixed sea ice and open water conditions, scatterometers being more inclusive regarding the detection of lower concentration and summer ice. The Bayesian algorithm for sea ice detection with ASCAT is currently able to produce daily global Arctic and Antarctic sea ice extents on 12.5 km polar stereographic grids (and 50 km resolution) filled with indicative sea ice age/thickness values. A salient feature of this algorithm is its excellent year-round agreement with QuikSCAT, offering a smooth continuation to the existing scatterometer sea ice extent record. The observed sea ice backscatter values at C-band show some loss of contrast between thin and thick ice types relative to the Ku-band QuikSCAT, but offer a better sensitivity to sea ice with prominent surface features such as fragmented marginal ice. It is the goal of this application to present a new sea ice edge product with a proxy for sea ice age that complements the standard record of sea ice extent and concentration currently provided by satellite radiometers. The ASCAT sea ice product proves to have better detection capabilities than radiometers during the summer months, providing an accurate and reliable description of the polar cap

extent for screening purposes, and offers potential for the creation, along with the QuikSCAT sea ice product, of a seamless long time record of sea ice extents that go back to 1999. For future work, the authors envision the generation of ASCAT sea ice extents at 25 km resolution, and the implementation of this methodology to backscatter collected from the Indian Ku-band dual-polarization Oceansat-2 scatterometer.

REFERENCES

[1] Comiso, J. C., Parkinson, C. L, Gersten, R., Stock, L., "Accelerated decline in the Arctic sea ice cover", Geophys. Res. Lett., 35, 2008.

[2] Stroeve, J., Maslanik, J., Serreze, M.C., Rigor, I., Meier, W., Fowler, C., "Sea ice response to an extreme negative phase of the Arctic Oscillation during winter 2009/2010", *Geophys. Res. Lett.*, 38, L02502, doi:10.1029/2010GL045662, 2011.

[3] Wu, Q., Zhang, X., "Observed forcing-feedback processes between Northern Hemisphere atmospheric circulation and Arctic sea ice coverage", *J. Geophys. Res.*, 115, D14119, doi:10.1029/2009JD013574, 2010.

[4] Kurtz, N. T., Markus, T., Farrell, S. L., Worthen, D. L., Boisvert, L. N., "Observations of recent Arctic sea ice volume loss and its impact on ocean-atmosphere energy exchange and ice production", *J. Geophys. Res.*, 116, C04015, doi:10.1029/2010JC006235, 2011.

[5] Budikova, D., "Role of Arctic sea ice in global atmospheric circulation: A review" Global and Planetary Change, 68, pp 149-163, 2009.

[6] Chelton, D.B., Freilich, M.H., "Scatterometer-based assessment of 10-m wind analyses from the operational ECMWF and NCEP numerical weather prediction models", Mon. Wea. Rev., 133, 409-429, 2005.

[7] English, S.J., "The importance of accurate skin temperature in assimilating radiances from satellite sounding instruments", IEEE Trans. Geosci. Remote Sens., Vol.46, No.2, pp. 403-408, 2008.

[8] Wang, M., Shi, W., "Detection of ice and mixed ice-water pixels for MODIS ocean color data processing", IEEE Trans. Geosci. Remote Sens., Vol.47, No.8, 2009.

[9] Tran, N., Girard-Ardhuin, F., Ezraty, R., Feng, H., Femenias, P., "Defining a sea ice flag for ENVISAT Altimetry Mission", IEEE Geosci. Rem. Sens. Lett., Vol.6, No.1, 2009.

[10] Cavalieri, D., Parkinson, C., Gloersen, P., Comiso, J., Zwally, H., "Deriving long term time series of sea ice cover from satellite passive microwave multisensor data sets", J. Geophys. Res., 104(C), 15803-15814, 1999.

[11] Anderson, H.S., Long, D., "Sea ice mapping method for SeaWinds", IEEE Trans. Geosci. Remote Sens., Vol.43, No.3, 647-657, 2005.

[12] Belmonte Rivas, M., Stoffelen, A., "New Bayesian algorithm for sea ice detection with QuikSCAT", IEEE Trans. Geosci. Remote Sens., doi: 10.1109/TGRS.2010.2101608, 2011.

[13] Nghiem, S.V., Clemente-Colon, P., "Arctic sea ice mapping with satellite radars", IEEE Aerospace and Electronic Systems Magazine, Vol.24, No.11, 41-44, 2009.

[14] Markus, T., Cavalieri, D., "An enhancement of the NASA team sea ice algorithm", IEEE Trans. Geosci. Remote Sens., Vol.38, No.3, 1387-1398, 2000.

[15] Cavalieri, D.J., Markus, T., Hall, D.K., Ivanoff, A., Glick, E., "Assessment of AMSR-E Antarctic winter sea-ice concentrations using Aqua MODIS", IEEE Trans. Geosci. Remote Sens., Vol.48, No.9, 3331-3339, 2010.

[16] Figa-Saldaña, J., Wilson, J.J.W., Attema, E., Gelsthorpe, R., Drinkwater, M.R., Stoffelen, A., "The Advanced Scatterometer (ASCAT) on the meteorological operational (MetOp) platform: A follow on for European wind scatterometers", *Can. .J. Remote Sensing*, Vol.28, No.3, pp.404-412, 2002.

[17] Hersbach, H., Stoffelen, A., de Haan, S., "An improved C-band scatterometer ocean geophysical model function: CMOD5", *J. Geophys. Res.*, 112, C03006, doi:10.1029/2006JC003743, 2007.

[18] Stoffelen, A., Portabella, M., "On Bayesian scatterometer wind inversion", IEEE Trans. Geosci. Remote Sens., Vol.44, No.6, 1523-1533, 2006.

[19] Cavalieri, D., and J. Comiso, "AMSR-E/Aqua Daily L3 12.5 km Tb, Sea Ice Conc., & Snow Depth Polar Grids V001", March to June 2004. Boulder, CO, USA: National Snow and Ice Data Center. Digital media, 2004.

[20] Wang, X.L., Swail, V.R., Zwiers, F.W., "Climatology and changes of extratropical cyclone activity: Comparison of ERA-40 with NCEP-NCAR reanalyses for 1958-2001", J. Climate, Vol.19, No.13, 3145-3166, 2006.

[21] Haarpainter, J., Spreen, G., "Use of Enhanced-Resolution QuikSCAT/SeaWinds Data for Operational Ice Services and Climate Research: Sea Ice Edge, Type, Concentration, and Drift", IEEE Trans. Geosci. Rem. Sens., Vol. 45, No. 10, pp. 3131-3137, 2007.

[22] Haarpainter, J., Tonboe, R.T., Long, D.G., VanWoert, M. L., "Automatic Detection and Validity of the Sea Ice Edge: An Application of Enhanced Resolution QuikScat/SeaWinds Data," IEEE Trans. Geosci. Rem. Sens., Vol. 42, No. 7, pp. 1433-1443, 2004.

[23] Early, D.S., Long, D.G., "Azimuth Modulation of C-band Scatterometer sigma-0 Over Southern Ocean Sea Ice," IEEE Trans. Geosci. Rem. Sens., Vol. 35, No. 5, pp. 1201-1209, 1997.

[24] Gohin, F., "Some active and passive microwave signatures of Antarctic sea ice from mid-winter to spring 1991", Int. J. Remote Sensing, vol. 116 (n.11), pp 2031-2054, 1995.

[25] Meier, W., Stroeve, J., "Comparison of sea ice extent and ice-edge location estimates from passive microwave and enhanced resolution scatterometer data", Ann. Glaciology, No. 48, pp. 65-70, 2008.

[26] Verspeek, J., Stoffelen, A., Portabella, M., Bonekamp, H, Anderson, C., Saldana, J.F., "Validation and calibration of ASCAT using CMOD5.n", IEEE Trans. Geosci. Rem. Sens., Vol. 48, No. 1, pp. 385-395, 2010.